THE JOURNAL OF PHYSICAL CHEMISTRY C
A JOURNAL OF THE AMERICAN CHEMICAL SOCIETY

pubs.acs.org/JPCC

Article

Recognition and Evaporation Monitoring of Micro-Droplet VOCs Based on CVD-Grown Monolayer MoS_2 through a Dielectric Screening Effect

Qiwei Zhang, Zeqian Ren, Rong Ma, Xiu Li, Lixia Guo, Jizhou Wu, Yuqing Li, Wenliang Liu, Peng Li, Yongming Fu,* and Jie Ma*

Cite This: *J. Phys. Chem. C* 2022, 126, 15864−15872

Read Online

ACCESS | Metrics & More | Article Recommendations | Supporting Information

ABSTRACT: Herein, an optical evaporation sensor is achieved based on the photoluminescence (PL) property of monolayer MoS_2 through the micro-droplet dielectric screening effect. The emission intensity, full width at half-maximum, photon energy, and intensity ratio of two excitons are related to the dielectric constant of the micro-droplets, which are employed to recognize the kind of liquids. During the evaporation process of volatile organic compound micro-droplets, the collected PL intensity is significantly affected by the refractive index. The theoretical model of a micro-droplet evaporation sensor based on the dielectric screening effect is established and verified by the finite-difference time-domain and the finite-element method. This work processes a fluorescent probe technique for micro-droplet recognition and evaporation monitoring with non-contact, high precision, and miniaturization.

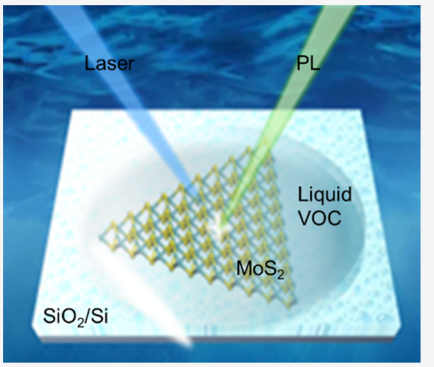

1. INTRODUCTION

Liquid level and evaporation sensors are widely used in meteorological observation, plant cultivation, healthcare, security, transportation, and geological survey.[1−3] The traditional evaporation sensors are fabricated by directly weighing the mass variation of the liquid. In the past years, several techniques have been developed to improve the accuracy and convenience of evaporation measurements, such as liquid-level measure, mechanical resonator, microelectromechanical systems, optical fibers, and gas sensors.[4−8] However, these evaporation sensors are not suitable for monitoring the evaporation of trace liquids, failed to recognize the kinds of liquid, and are easily disturbed by the electromagnetic environment. To meet the modern internet of things development, there is an urgent requirement to further develop evaporation sensors with high precision, communication, and miniaturization.

Optical techniques have exhibited good innovation and application in environmental sensing and biological monitoring due to their advantages of non-contact and non-destructive measurement, strong anti-interference ability, and high-speed transmission.[9−11] Among the optical sensing techniques, the fluorescence probe method based on optical fibers, metal nanoparticles, quantum dots, and polymers has been utilized in bioimaging, explosive detection, temperature monitoring, and liquid analysis.[12−15] However, the traditional fluorescence probe materials are not applicable enough for evaporation sensing applications, and developing novel fluorescent probes is necessary.

Monolayer transition-metal dichalcogenides (TMDCs) are two-dimensional (2D) hexagonal crystals composed of triple atomic layers, which have drawn enormous attention due to their interesting electronic, optical, and mechanical properties.[16] Particularly, monolayer MoS_2 exhibits high room-temperature excitonic binding energy, low dielectric screening effect, and spin−orbit coupling (SOC).[17] The optical transition reflects the behavior of excitons which are intensively influenced by the environmental dielectric screening effect. Previous works have reported that environmental dielectrics strongly influence the electrical and optical properties of monolayer MoS_2.[18−22] Ma and Jena studied the relationship between the carrier transport characteristics, environmental medium, and impurity density of monolayer MoS_2, revealing that electron mobility is mainly determined by the scattering of charged impurities.[21] Buscema et al. attributed the variation of exciton energy to substrate-induced strain and doping by studying the Raman and photoluminescence (PL) spectra of monolayer MoS_2 on different substrates.[22] Although mono-

Received: August 6, 2022
Revised: August 26, 2022
Published: September 7, 2022

https://doi.org/10.1021/acs.jpcc.2c05598
J. Phys. Chem. C 2022, 126, 15864−15872

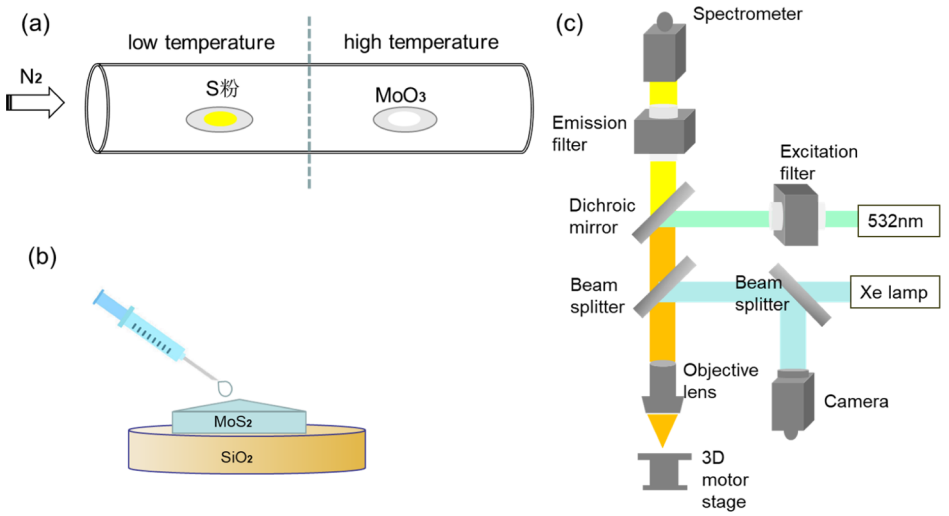

Figure 1. Schematic diagrams of the experimental sets for (a) CVD growth of monolayer MoS_2, (b) dropping VOC micro-droplets on monolayer MoS2, and a (c) home-made laser scanning confocal microscope.

layer TMDCs exhibit application potential in environmental monitoring through the dielectric screening effect, research studies on exciton-related optical properties are still lacking in the current stage.

In this paper, the evaporation sensor is achieved based on the PL property of monolayer MoS_2 through the micro-droplet dielectric screening effect. The MoS_2 crystal with a monolayer structure is synthesized using the chemical vapor deposition (CVD) method. The peak intensity, position, full width at half-maximum (FWHM), and intensity ratio of PL spectra are related to the environmental liquid dielectric constant. The evaporation sensing properties are determined by measuring the time-dependent PL spectra after dropping 3 μL of liquid on the monolayer MoS_2. The finite-difference time-domain (FDTD) method is used to simulate the scatting electromagnetic field, and the detailed relationship between PL parameters and the environmental dielectric constant is also qualitatively examined. In addition, the time-dependent PL characters of monolayer MoS_2 after covering micro-droplets are also observed and discussed by the finite-element method (FEM), which demonstrates the application potential as a liquid evaporation sensor for recognizing and sensing various volatile organic compounds (VOCs). This work proposes a novel evaporation sensing strategy for micro-droplets and expands the application field of fluorescent probe sensors.

2. EXPERIMENTAL SECTION

2.1. Synthesis of Monolayer MoS_2 Using the CVD Method. Monolayer MoS_2 was synthesized in a horizontal tube furnace equipped with a 2 inch-diameter quartz tube using MoO_3 and S as solid precursors. Typically, 0.01 g of MoO_3 powder (99.9%, Sigma-Aldrich) was placed in the middle region, and 0.5 g of sulfur powder (99.5%, Sinopharm) was placed 20 cm behind the first alumina boat. The pre-cleaned SiO_2/Si substrate was covered in an inverted manner on the second alumina boat, above the MoO_3 powder. The quartz tube was pre-evacuated to 10 Pa and then flushed using ultra-pure N_2 gas until reaching 10^5 Pa. This process was repeated three times to remove the oxygen and other contamination from the quartz tube, followed by passing over N_2 gas with a flow rate of 70 sccm. Subsequently, the quartz tube was heated to 810 °C with a heating rate of 15 °C min^{-1}, and S powder was spontaneously heated by the residual temperature. After maintaining at 810 °C for 20 min, the tube furnace was turned off, and the tube was cooled naturally down to room temperature.

2.2. Characterization and Measurements. The morphology of monolayer MoS_2 was observed by scanning electron microscopy (SEM, EM 30+, COXEM) and optical microscopy. The altitude mapping profile around the edge region of monolayer MoS_2 was measured by atom force microscopy (AFM, NT-MDT, NTEGRA Spectra). The PL spectra of monolayer MoS_2 were obtained by a homemade laser scanning confocal microscope at room temperature under different liquid environments. The exciting light was provided by a CW laser (532 nm, 20 mW) and focused to a 1 μm-spot on monolayer MoS_2 using a 50× M PLAN semi-apochromat objective lens (LMPLFLN 50×, Olympus) with a long work distance of 10.6 mm. The optical spectrum was collected by a linear-array charge-coupled device equipped with a 300-line grating. To investigate the influence of the environmental dielectric screening effect on the excitonic emission, the screened PL spectrum was measured after dropping 3 μL of liquid on the monolayer MoS_2 and waiting 30 s for spreading. The dielectric constants of the VOC droplets were directly measured using the capacitance method by dropping the liquid VOC on a micro-electrode pair. To monitor the evaporation process, the spectra were collected at 1, 2, 3, and 10 min after dropping, respectively. After evaporation measurements, the monolayer MoS_2 was heated to 80 °C for 10 min to completely eliminate the liquid VOCs. Conventional evaporation measurements were carried out in an open environment with 30% RH humidity, and the higher ambient humidity was controlled naturally by the rainy climate without human intervention.

2.3. Modeling. The FDTD simulation was applied to calculate the scattering field in different dielectric environments. The simulation model was composed of a 1 mm × 1 mm × 0.1 mm cuboid SiO_2/Si/substrate, a trilateral MoS_2 with a side length of 30 μm and a thickness of 0.6 nm, and a cylinder liquid model with a thickness of 0.5 mm covering the MoS_2 triangle. The incident light was simulated by a vertical incidence full-field scattering light source. By placing various surveillance flats on the surface of monolayer MoS_2, the scattering spectrum and surface electric field distribution under

https://doi.org/10.1021/acs.jpcc.2c05598
J. Phys. Chem. C 2022, 126, 15864−15872

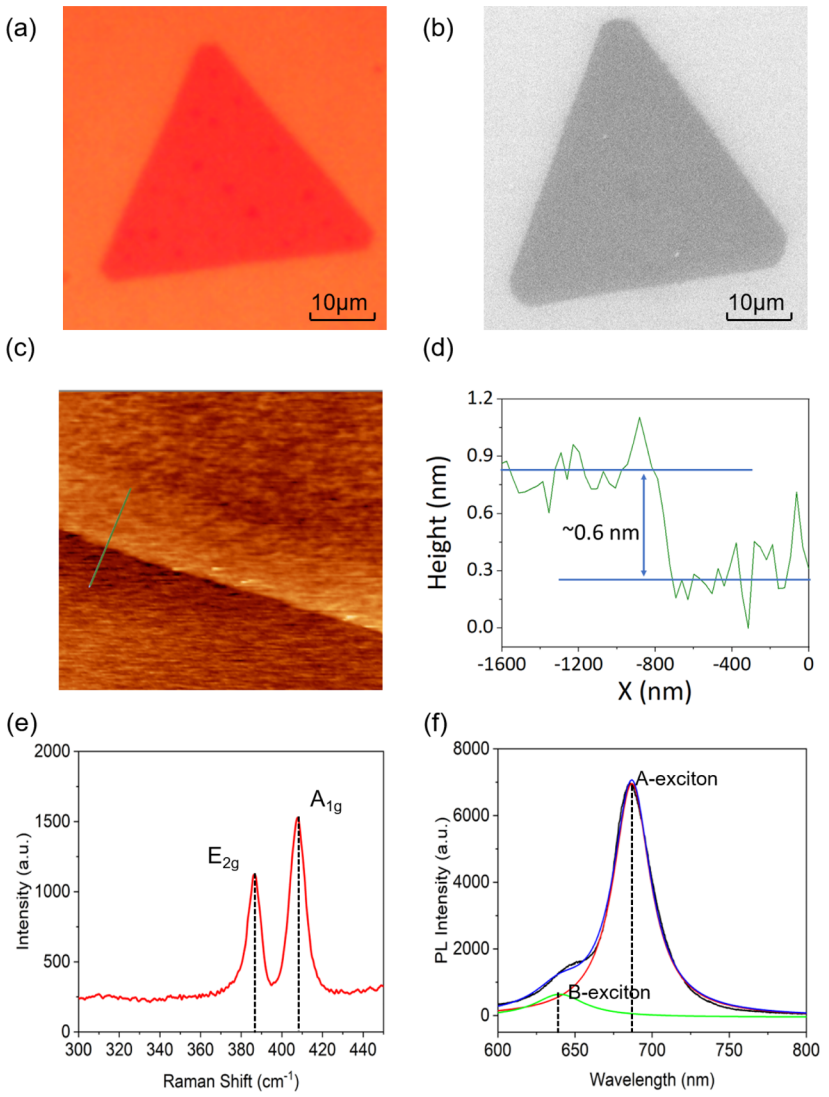

Figure 2. Morphology and layer structure of monolayer MoS_2. (a) Optical image. (b) SEM image. (c) Magnified AFM profile. (d) Altitude scanning profile. (e) Raman spectrum. (f) PL spectrum.

different liquid conditions were obtained. More parameter values can be seen from Table S1.

The FEM simulation was used to simulate the liquid spreading process to measure the film thickness and spreading radius of different liquids. 3 μL of liquid was modeled as a microsphere with a radius of 0.8 mm and an initial velocity of zero. The solid−liquid−gas environment was established by a multi-physical field consisting of a two-phase flow model and a wetted wall model. The surface tension coefficient and contact angle provided the necessary parameters for simulation (specific parameters were provided by the material library). The film thickness and spreading radius were measured from the fluid volume fraction diagram.

3. RESULTS AND DISCUSSION

3.1. Conception of Monolayer MoS_2-Based Evaporation Sensors. The monolayer MoS_2 is synthesized in a horizontal tube furnace (Figure 1a). Before the test, 3 μL of a micro-droplet is dropped on the monolayer MoS_2 (Figure 1b). Then, the PL spectrum of monolayer MoS_2 is measured using a laser confocal microscope (Figure 1c), which is significantly affected by the environment dielectric constant. By dropping liquids with different dielectric constants, the intensity and position of the PL peak correspondingly change, which is employed to identify the type of liquids. Moreover, the intensity ratio of two PL peaks also varies with liquid dielectric constant for improving the identification accuracy. During the evaporation process, the thickness of the dropped liquid gets thinner with time, leading to the gradually decreasing dielectric screening effect. To test the evaporation sensing performance, ethanol, acetone, and methanol are selected as the representative liquid VOCs due to their discrepant dielectric constants, where the detailed parameters of the VOCs are shown in Table S1.

The optical photograph and SEM image of the synthesized sample are shown in Figure 2a,b, respectively. The morphology of a CVD-synthesized MoS_2 crystal is a flat rounded triangle with a side length of ~30 μm. Figure 2c shows a magnified AFM altitude mapping profile at the edge region of the triangle, displaying the smooth and sharp edge. The altitude variation is measured by scanning perpendicular to the edge, proving that the thickness is ~0.6 nm, in good agreement with monolayer MoS_2 (Figure 2d). As shown in the Raman spectrum (Figure 2e), the two peaks located at 386 and 407

https://doi.org/10.1021/acs.jpcc.2c05598
J. Phys. Chem. C 2022, 126, 15864−15872

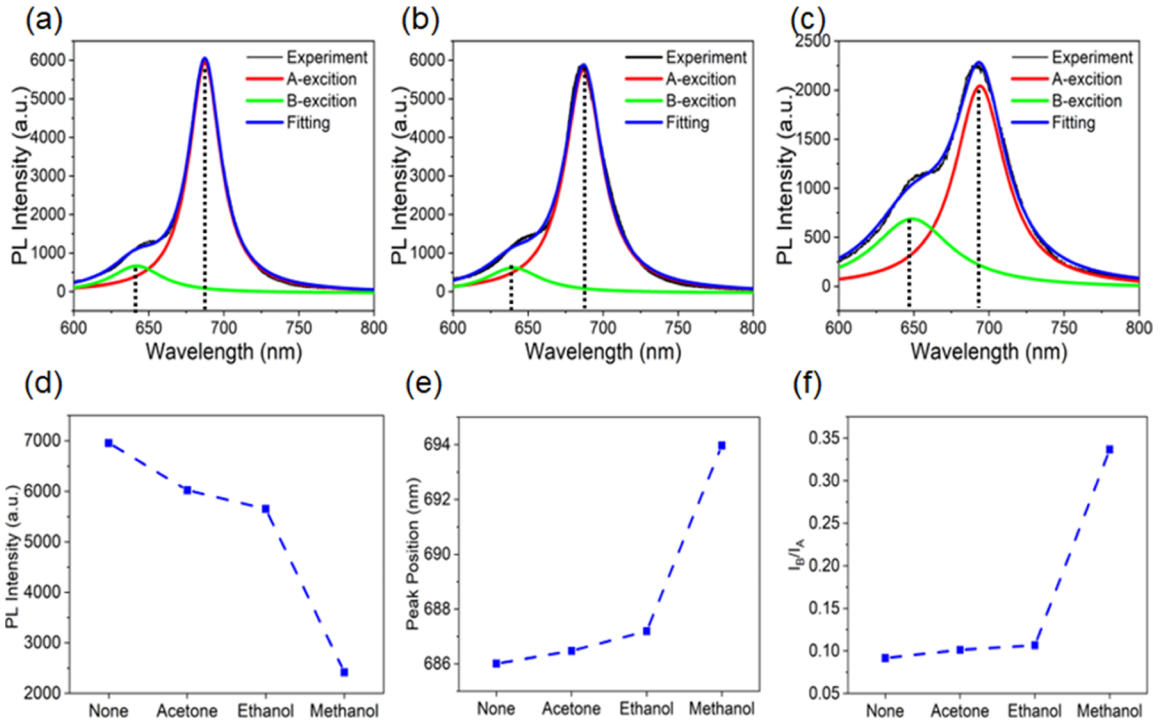

Figure 3. (a–c) Typical PL energy spectra of monolayer MoS_2 covered by (a) acetone, (b) ethanol, and (c) methanol. (d–f) Comparison of the (d) A-exciton intensity, (e) A-exciton peak position, and (f) B/A intensity ratio under different liquid VOC environments.

cm^{-1} belong to the in-plane vibration E_{2g}^1 and out-of-plane vibration (A_{1g}), respectively, further indicating the monolayer property of MoS_2 on the SiO_2/Si substrate. Figure 2f shows a typical PL spectrum of monolayer MoS_2 in an atmosphere environment. The PL spectrum is well divided into two peaks located at 1.80 and 1.93 eV by Lorentz's formula, corresponding to the A-exciton and B-exciton, respectively.[23] The large energy splitting between the A-exciton and B-exciton proves the strong SOC.

3.2. PL Property under Different Liquid Conditions. To investigate the influence of the micro-droplet liquid environment on PL emission, the PL spectra are measured by dropping ethanol, methanol, and acetone on monolayer MoS_2, respectively (Figure 3a–c). The PL spectra are compared in Figure S1, and the analytic results are shown in Figure 3d–f. For the major peak, with the increasing liquid dielectric constant in the order of acetone (20.7), ethanol (24.6), and methanol (32.6), the PL spectra display remarkable changes. The peak intensity decreases (Figure 3d), the FWHM increases (Figure S2), and the peak position red-shifts (Figure 3e) with increasing dielectric constant, which implies that the environmental dielectric constant has a significant impact on the formation and emission of the excitons in monolayer MoS_2. After the peak splitting calculation, the spectra under liquid environments still maintain the linear superposition characteristics of A-exciton and B-exciton. By analyzing the variation tendency of the intensity ratios of A-exciton and B-exciton, it is found that the B/A intensity ratio also varies with the dielectric constant (Figure 3f). To further verify the contribution of the dielectric constant to the decreased exciton emitting rate, 3 μL of deionized water is dropped on the monolayer MoS_2 (Figure S3). The PL intensity is rapidly annihilated since the dielectric constant of water is as high as 78.6. These results suggest that measuring the peak position and intensity of the PL spectrum of monolayer MoS_2 is a rational strategy for liquid recognition.

3.3. Mechanism of the Micro-Droplet Dielectric Screening Effect. The relationship between the exciton emission and micro-droplet dielectric constant is preliminarily attributed to the dielectric screening effect. First, the mechanism of dielectric-screened exciton energy is discussed for peak shift. As reported in the previous literature, the emission energy (E) is highly related to the environmental dielectric constant (ε_r) and refractive index (n), as described by eq 1[19]

$$E \propto -(\alpha_e - \alpha_g)[f(\varepsilon_r) - f(n^2)] \quad (1)$$

where α_e and α_g are the polarizabilities of the excited state and ground state, respectively. The item $f(\varepsilon_r) - f(n^2)$ is the difference in Onsager polarity functions responsible for different interaction terms, such as dipole–dipole interaction and dispersion interaction. Methanol, ethanol, and acetone are polar solvents, which display a larger dielectric screening effect than non-polar solvents. The stability of the excited state in polar solvents is better; it is similar to the observed red shift of the transition energy for quantum dots and carbon nanotubes in polar solvents. The emission energy decreases with the increasing value of $f(\varepsilon_r) - f(n^2)$, and the PL peak red-shifts.

Second, the mechanism of dielectric screened excitonic emission is discussed for the variations of peak intensity and width. The peak intensity of photon emission can be interpreted as the occurrence probability (P) of particles at the corresponding wavelength, which is represented by the square modulus of the wave function inferred by the hydrogen-like atom model. A Schrodinger equation that satisfied the electron state wave function in the hydrogen-like atom is established by substituting the Laplace operator and coulomb

https://doi.org/10.1021/acs.jpcc.2c05598
J. Phys. Chem. C 2022, 126, 15864–15872

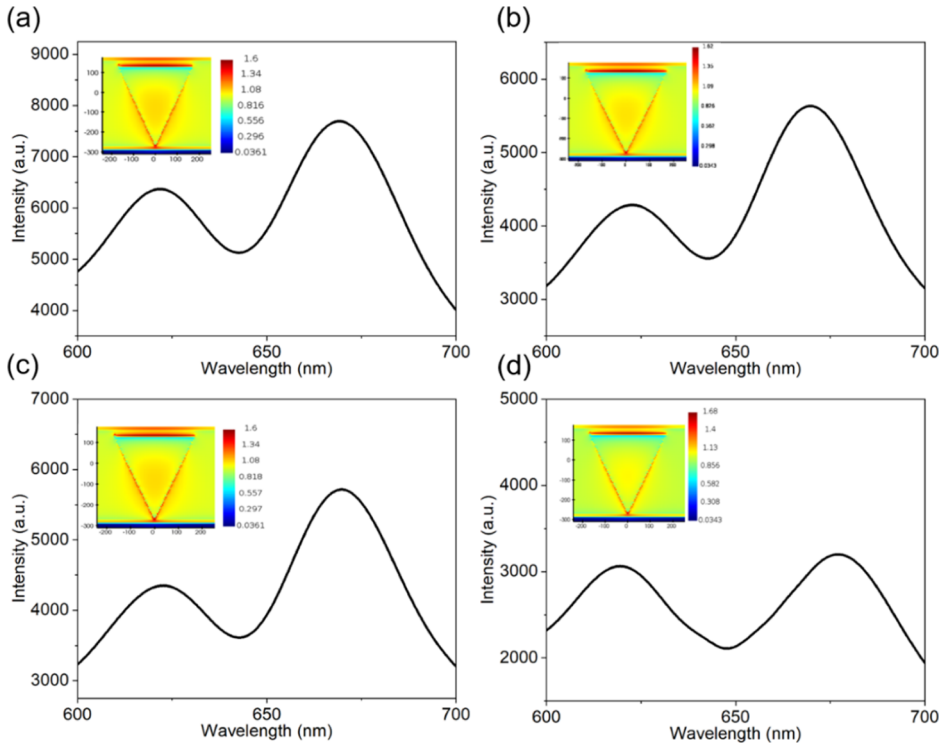

Figure 4. FDTD simulations of a monolayer MoS_2 on a SiO_2/Si wafer covered with (a) air, (b) acetone, (c) ethanol, and (d) methanol.

force. Equation 2 is the Schrodinger equation in a polar coordinate

$$\frac{1}{r^2}\left[\frac{\partial}{\partial r}\left(r^2\frac{\partial}{\partial r}\right) + \frac{1}{\sin\theta}\frac{\partial}{\partial\theta}\left(\sin\theta\frac{\partial}{\partial\theta}\right) + \frac{1}{\sin^2\theta}\frac{\partial^2}{\partial\varphi^2}\right]\psi + \frac{2\pi^2 m}{\hbar^2}\left(E + \frac{Ze^2}{4\pi r}\right)\psi = 0 \tag{2}$$

where m, Z, and e are the magnetic quantum number, equivalent atomic number, and electron charge, respectively. The detailed radial wave function $R_{nl}(r)$ is expressed as eq 3 through separation of variables

$$R_{nl}(r) = \sqrt{\frac{(n-l-1)!}{2n(n+l)!}\left(\frac{2Z}{na\varepsilon_r}\right)^3}\left(\frac{2Zr}{na\varepsilon_r}\right)^l L_{n-l-1}^{2l+1}\left(\frac{2Zr}{na}\right) e^{-Zr/na\varepsilon_r} \tag{3}$$

where n is the principal quantum number, l is the orbital angular momentum quantum number, a is the Bohr radius of the hydrogen-like atom, and L is the associated Laguerre polynomial, respectively. Since the photon emission is mainly dominated by the ground state, n and l are assigned as 1 and 0, respectively. Equation 3 is simplified to eq 4

$$R_{10}(r) = 2\left(\frac{Z}{a\varepsilon_r}\right)^{3/2} e^{-Zr/a\varepsilon_r} \tag{4}$$

which infers that $P \propto |rR_{10}(r)|^2$ is exponentially related to ε_r with a monotone subtraction under a polar solvent liquid environment. The occurrence probability of the quasiparticles at the corresponding wavelength decreases with increasing ε_r, leading to the peak intensity in the PL spectrum decreasing accordingly. On the other hand, the higher environment ε_r enhances the scattering between the excitons and the charged impurities at the MoS_2/liquid interface.[24−26] Thus, the lifetime of the excitons in monolayer MoS_2 is efficiently extended. As a result, the peak width increases with the increasing ε_r since the peak width is proportional to the lifetime of excitons.

Third, the intensity ratio of B-exciton and A-exciton is also turned by the environment dielectric constant. The A-exciton and B-exciton intensity radio is expressed as eq 5 through the mass action model[18]

$$\frac{I_B}{I_A} = \frac{\Gamma_B}{\Gamma_A}\frac{N_B}{N_A} \tag{5}$$

where N_A (N_B) and Γ_A (Γ_B) are the density and radiative recombination rate of A-exciton (B-exciton), respectively. Similar to other low-dimensional systems, the radiative recombination of the excitons in monolayer MoS_2 is also influenced by the environment dielectrics. The radiative recombination rate is followed the power function of the environment dielectric constant, as shown in eq 6

$$\frac{\Gamma_A}{\Gamma_B} = K(\kappa_{eff})^{\delta} \tag{6}$$

where K and δ are the linear and exponential fitting parameters related to the effective environmental dielectric constant (κ_{eff}), respectively. Accordingly, the B/A intensity ratio is described in eq 7

$$\frac{I_B}{I_A} = K(\kappa_{eff})^{\delta}\exp\left(-\frac{\varepsilon_B - \varepsilon_A + \Delta}{k_B T}\right) \tag{7}$$

where ε_A and ε_B donate the binding energy of the A-exciton and B-exciton, Δ represents the valence band splitting, and $k_B T$ is the thermal energy, respectively. Therefore, the B/A intensity ratio is incremental with the dielectric constant of the micro-droplet.

https://doi.org/10.1021/acs.jpcc.2c05598
J. Phys. Chem. C 2022, 126, 15864−15872

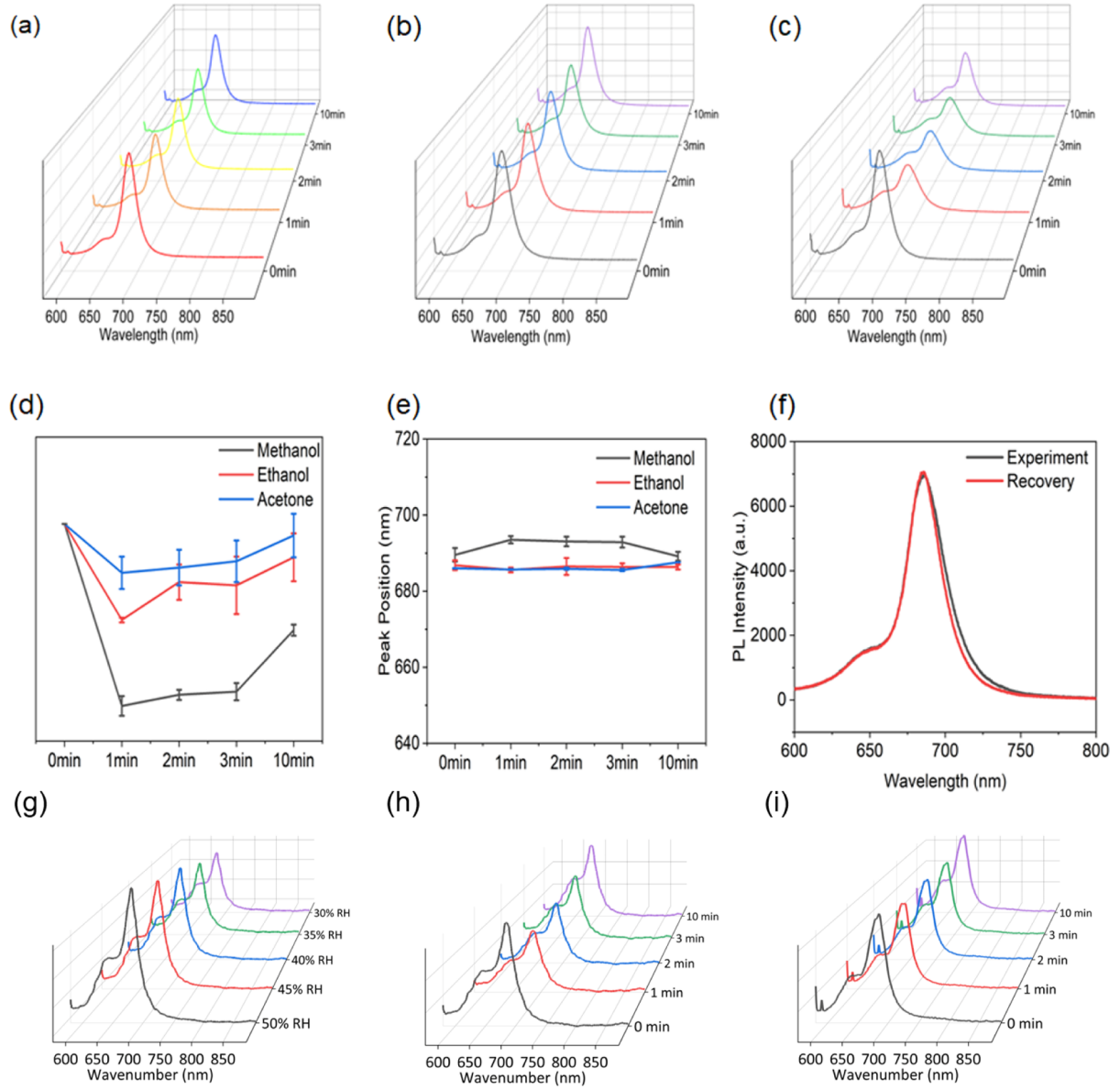

Figure 5. PL spectra of monolayer MoS_2 during the evaporation process. (a−c) PL spectra 1, 2, 3, and 10 min after covering with micro-droplets of (a) ethanol, (b) acetone, and (c) methanol. (d) Intensity comparison of A-excitons. (e) Peak position comparison of A-excitons. (f) PL spectra of monolayer MoS_2 before and after the evaporation process. (g) PL spectra under various humidities. (h,i) PL spectra during the ethanol evaporation process under air humidity of (h) 40% RH and (i) 50% RH.

3.4. Simulations. The FDTD method has been widely used in the research fields of micro−nano optics, near-field optics, photonic crystals, and so forth.[27−29] Herein, FDTD is utilized to prove the proposed mechanism by simulating the scattering spectra of monolayer MoS_2 in different liquid environments through establishing a full-field scattering light source and scattering cross section. The scattering spectra display similar exciton characteristics with fluorescence spectra, as shown in Figure 4.[30] Figure 4a−d shows the simulated scattering spectra of monolayer MoS_2 under air, ethanol, methanol, and acetone, respectively, displaying that the A-exciton peak in simulated scattering spectra red-shifts with increasing dielectric constant. The insets are the corresponding surface electric fields of monolayer MoS_2, indicating that the surface electrical field is significantly screened by the environmental dielectric constant. The comparison of different scattering spectra is shown in Figure S4, which agrees well with the experimental results. These simulation results confirm the proposed mechanism that the environmental condition can affect the exciton population and optical emission by the dielectric screening effect.

3.5. Evaporation Sensing Investigation. Ethanol, methanol, and acetone are VOCs that can spontaneously evaporate at room temperature due to their boiling points, which are lower than 80 °C. The droplet thickness gradually decreases with evaporation, which may affect the PL measurements. As shown in Figure 5a−c, the PL intensities correspondingly increase with evaporation-induced decrease of thickness, which implies the potential application as an evaporation sensor. The increasing rates of PL intensities also follow positive correlations to the liquid dielectric constant during evaporation under different liquid micro-droplets (Figure 5d). The peak position and FWHM remain almost constant with increasing time (Figures 5e and S5), indicating

https://doi.org/10.1021/acs.jpcc.2c05598
J. Phys. Chem. C 2022, 126, 15864−15872

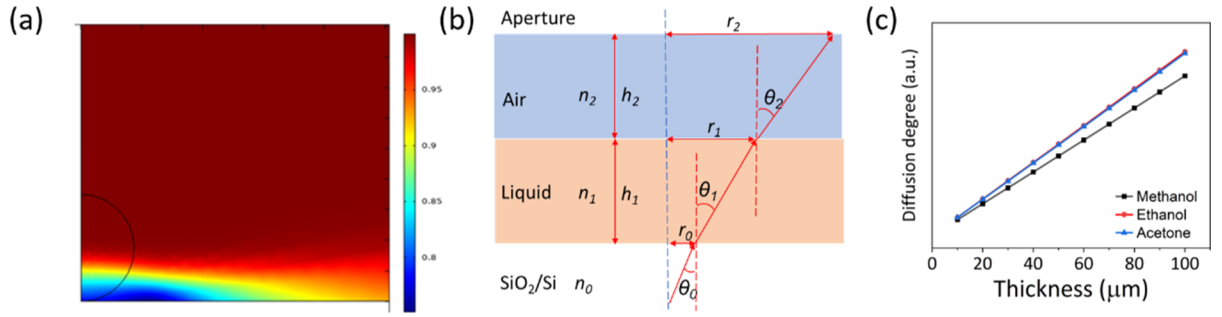

Figure 6. Diagramed mechanism of the micro-droplet evaporation sensing process. (a) FEM simulation of micro-droplet spread. (b) Light refraction crossing the liquid film. (c) Calculated relationship between thickness and diffusion degree.

that the dielectric screening effect is not significantly affected during the evaporation. Thus, the recognition function is retained in the evaporation process. It is noted that the FWHM of methanol is unstable. To further discuss this abnormal phenomenon, the methanol−water mixture with different concentrations is dropped on the monolayer, where the PL intensity decreases with increasing methanol concentration (Figure S6). The phenomenon implies that other mechanisms may occur during the evaporation process of methanol beyond the dielectric screening effect, which has not been solved in this work. After eliminating the VOCs, the PL spectra can recover to the initial level with a high overlap ratio (Figures 5f, S7, and S8), which illustrates the good stability and repeatability of the evaporation sensor. To study the influence of water vapor, the PL spectra of monolayer MoS_2 without the VOC droplet are measured under varying ambient humidities, as shown in Figure 5g. Interestingly, the PL intensity increases with increasing humidity. The ethanol evaporation processes are also measured under 40 and 50% RH, as shown in Figure 5h,i, respectively. The recovery rate of PL intensity also increases with increasing humidity, indicating that the high ambient humidity can accelerate the VOC evaporation process but does not significantly affect the sensing characteristics of monolayer MoS_2.

3.6. Evaporation Sensing Mechanism. The thickness of the liquid film plays an important role in PL detection during evaporation. When the micro-droplets are dropped onto the monolayer MoS_2 on a SiO_2/Si wafer, the micro-droplets quickly spread out over time and eventually form thin films. The spreading process of water is simulated by FEM (Figure 6a), displaying a disc-like film with a maximum thickness of ∼100 μm. The thicknesses of the liquid films are experimentally measured to ∼100 μm (Table S2), similar to the simulation result, indicating the weak dependence of liquid viscosity, surface tension, and refractive index on the spreading of micro-droplets due to the high wettability of SiO_2. For the propagation and collection of PL light during the evaporation process, the absorption, scattering, and refraction may contribute to the thickness-dependent intensity. In this case, the effects of absorption and scattering can be ignored due to the merely micrometer-scale thickness, while the refraction dominates the PL measurements. When the PL light of monolayer MoS_2 is emitted into the air through the liquid film, the light propagation follows the law from the light-dense medium to the light-phobic medium wherein the light propagation path is deflected away from the interface normal (Figure 6b). The equation set is shown as follows

$$n_0 \sin\theta_0 = n_1 \sin\theta_1 = n_2 \sin\theta_2 \tag{8}$$

$$\tan\theta_1 = (r_1 - r_0)/h_1 \tag{9}$$

$$\tan\theta_2 = (r_2 - r_1)/h_2 \tag{10}$$

where θ, r, h, and n represent the maximum angular separation, radius, thickness, and refraction index, while the labels 0, 1, and 2 represent SiO_2, liquids, and air, respectively. The equation set is transformed to eq 11 by assuming the refractive index of air (n_2) with 1

$$r_2 = h_2 \tan[\arcsin(n_0 \sin\theta_0)] + h_1 \tan[\arcsin(n_0 \sin\theta_0/n_1)] + r_0 \tag{11}$$

where $h_1 + h_2$ approximates the work distance of the objective lens. The relationship between the diffusion degree and liquid thickness (h_1) is dissolved, as shown in Figure 6c. The deflection degree is proportional to the thickness (optical path) and refractive index of the liquid film. The effective PL energy flux density collected by the objective lens is inversely proportional to the square of r_2. Thus, as evaporation progresses, the thickness of the liquid film gradually decreases, causing more light to enter the objective lens for stronger PL intensity measurement.

4. CONCLUSIONS

In summary, the relationship between the exciton emission property of monolayer MoS_2 and the environmental dielectric constant of micro-droplets is systematically investigated. Based on the environmental dielectric screening effect, a new approach is presented for the recognition and evaporation monitoring of liquid VOCs. Compared with other evaporation sensors, the optical micro-droplet evaporation sensor exhibits the outstanding features of non-contact, high precision, anti-interference, and miniaturization. In future work, the evaporation sensor can be further improved by constructing 2D heterojunctions on flexible substrates.

■ ASSOCIATED CONTENT

Supporting Information

The Supporting Information is available free of charge at https://pubs.acs.org/doi/10.1021/acs.jpcc.2c05598.

Analysis of PL spectra; FDTD simulation results; PL spectra dependent on methanol concentration; PL spectra showing recovery; basic physical properties of the VOCs; and measured factors of VOC films (PDF)

https://doi.org/10.1021/acs.jpcc.2c05598
J. Phys. Chem. C 2022, 126, 15864−15872

AUTHOR INFORMATION

Corresponding Authors

Yongming Fu − *School of Physics and Electronic Engineering, State Key Laboratory of Quantum Optics and Quantum Optics Devices, Institute of Laser Spectroscopy, Shanxi University, Taiyuan 030006, China;* orcid.org/0000-0002-7543-4327; Email: fuyongming@sxu.edu.cn

Jie Ma − *School of Physics and Electronic Engineering, State Key Laboratory of Quantum Optics and Quantum Optics Devices, Institute of Laser Spectroscopy, Shanxi University, Taiyuan 030006, China; Collaborative Innovation Center of Extreme Optics, Shanxi University, Taiyuan 030006, China;* Email: mj@sxu.edu.cn

Authors

Qiwei Zhang − *School of Physics and Electronic Engineering, State Key Laboratory of Quantum Optics and Quantum Optics Devices, Institute of Laser Spectroscopy, Shanxi University, Taiyuan 030006, China*

Zeqian Ren − *School of Physics and Electronic Engineering, State Key Laboratory of Quantum Optics and Quantum Optics Devices, Institute of Laser Spectroscopy, Shanxi University, Taiyuan 030006, China*

Rong Ma − *School of Physics and Electronic Engineering, State Key Laboratory of Quantum Optics and Quantum Optics Devices, Institute of Laser Spectroscopy, Shanxi University, Taiyuan 030006, China*

Xiu Li − *School of Physics and Electronic Engineering, State Key Laboratory of Quantum Optics and Quantum Optics Devices, Institute of Laser Spectroscopy, Shanxi University, Taiyuan 030006, China*

Lixia Guo − *School of Physics and Electronic Engineering, State Key Laboratory of Quantum Optics and Quantum Optics Devices, Institute of Laser Spectroscopy, Shanxi University, Taiyuan 030006, China*

Jizhou Wu − *School of Physics and Electronic Engineering, State Key Laboratory of Quantum Optics and Quantum Optics Devices, Institute of Laser Spectroscopy, Shanxi University, Taiyuan 030006, China; Collaborative Innovation Center of Extreme Optics, Shanxi University, Taiyuan 030006, China*

Yuqing Li − *School of Physics and Electronic Engineering, State Key Laboratory of Quantum Optics and Quantum Optics Devices, Institute of Laser Spectroscopy, Shanxi University, Taiyuan 030006, China; Collaborative Innovation Center of Extreme Optics, Shanxi University, Taiyuan 030006, China*

Wenliang Liu − *School of Physics and Electronic Engineering, State Key Laboratory of Quantum Optics and Quantum Optics Devices, Institute of Laser Spectroscopy, Shanxi University, Taiyuan 030006, China; Collaborative Innovation Center of Extreme Optics, Shanxi University, Taiyuan 030006, China*

Peng Li − *School of Physics and Electronic Engineering, State Key Laboratory of Quantum Optics and Quantum Optics Devices, Institute of Laser Spectroscopy, Shanxi University, Taiyuan 030006, China;* orcid.org/0000-0001-8868-9743

Complete contact information is available at: https://pubs.acs.org/10.1021/acs.jpcc.2c05598

Notes

The authors declare no competing financial interest.

ACKNOWLEDGMENTS

This work was funded by the National Key R&D Program of China (grant no. 2017YFA0304203); the National Natural Science Foundation of China (grant nos. 62020106014, 62175140, 61901249, 92165106, 12104276); PCSIRT (grant no. IRT—17R70); 111 project (grant no. D18001); the Program for the Outstanding Innovative Teams of Higher Learning Institutions of Shanxi (OIT); the Applied Basic Research Project of Shanxi Province, China (grant nos. 201901D211191, 201901D211188); the Shanxi 1331 KSC; and the collaborative grant by the Russian Foundation for Basic Research and NSF of China (grant no. 62011530047, 20-53-53025 in the RFBR classification).

REFERENCES

(1) Cho, M. Y.; Kim, I. S.; Kim, S. H.; Park, C.; Kim, N. Y.; Kim, S. W.; Kim, S.; Oh, J. M. Unique Noncontact Monitoring of Human Respiration and Sweat Evaporation Using a $CsPb_2Br_5$-Based Sensor. *ACS Appl. Mater. Interfaces* **2021**, *13*, 5602−5613.

(2) Kano, S.; Kim, K.; Fujii, M. Fast-Response and Flexible Nanocrystal-Based Humidity Sensor for Monitoring Human Respiration and Water Evaporation on Skin. *ACS Sens.* **2017**, *2*, 828−833.

(3) Zhou, Q.; Zhang, S. P.; Li, Y. X.; Xie, C. S.; Li, H. Y.; Ding, X. H. A Chinese Liquor Classification Method Based on Liquid Evaporation with One Unmodulated Metal Oxide Gas Sensor. *Sens. Actuators, B* **2011**, *160*, 483−489.

(4) Arcamone, J.; Dujardin, E.; Rius, G.; Pérez-Murano, F.; Ondarçuhu, T. Evaporation of Femtoliter Sessile Droplets Monitored with Nanomechanical Mass Sensors. *J. Phys. Chem. B* **2007**, *111*, 13020−13027.

(5) Chen, X. M.; Li, Y. J.; Han, D.; Zhu, H. C.; Xue, C. D.; Chui, H. C.; Cao, T.; Qin, K. R. A Capillary-Evaporation Micropump for Real-Time Sweat Rate Monitoring with an Electrochemical Sensor. *Micromachines* **2019**, *10*, 457.

(6) Park, J.; Lee, S.; Kim, D. I.; Kim, Y. Y.; Kim, S.; Kim, H. J.; Kim, Y. Evaporation-Rate Control of Water Droplets on Flexible Transparent Heater for Sensor Application. *Sensors* **2019**, *19*, 4918.

(7) Park, K.; Kim, N.; Morisette, D. T.; Aluru, N. R.; Bashir, R. Resonant Mems Mass Sensors for Measurement of Microdroplet Evaporation. *J. Microelectromech. Syst.* **2012**, *21*, 702−711.

(8) Shimazaki, Y.; Katsuta, S. Spatiotemporal Sweat Evaporation and Evaporative Cooling in Thermal Environments Determined from Wearable Sensors. *Appl. Therm. Eng.* **2019**, *163*, 114422.

(9) Liu, T.; Pagliano, F.; van Veldhoven, R.; Pogoretskiy, V.; Jiao, Y.; Fiore, A. Integrated Nano-Optomechanical Displacement Sensor with Ultrawide Optical Bandwidth. *Nat. Commun.* **2020**, *11*, 2407.

(10) Song, E.; Chen, M.; Chen, Z.; Zhou, Y.; Zhou, W.; Sun, H.-T.; Yang, X.; Gan, J.; Ye, S.; Zhang, Q. Mn^{2+}-Activated Dual-Wavelength Emitting Materials toward Wearable Optical Fibre Temperature Sensor. *Nat. Commun.* **2022**, *13*, 2166.

(11) Werley, C. A.; Boccardo, S.; Rigamonti, A.; Hansson, E. M.; Cohen, A. E. Multiplexed Optical Sensors in Arrayed Islands of Cells for Multimodal Recordings of Cellular Physiology. *Nat. Commun.* **2020**, *11*, 3881.

(12) Asad, M.; Imran Anwar, M. I.; Abbas, A.; Younas, A.; Hussain, S.; Gao, R. X.; Li, L. K.; Shahid, M.; Khan, S. Aie Based Luminescent Porous Materials as Cutting-Edge Tool for Environmental Monitoring: State of the Art Advances and Perspectives. *Coord. Chem. Rev.* **2022**, *463*, 214539.

(13) Duffet, L.; Kosar, S.; Panniello, M.; Viberti, B.; Bracey, E.; Zych, A. D.; Radoux-Mergault, A.; Zhou, X. H.; Dernic, J.; Ravotto, L.; et al. A Genetically Encoded Sensor for in Vivo Imaging of Orexin Neuropeptides. *Nat. Methods* **2022**, *19*, 231−241.

(14) Ke, Y.; Liu, Y.; Zu, B. Y.; Lei, D.; Wang, G. F.; Li, J. G.; Ren, W. F.; Dou, X. C. Electronic Tuning in Reaction-Based Fluorescent Sensing for Instantaneous and Ultrasensitive Visualization of Ethylenediamine. *Angew. Chem., Int. Ed.* **2022**, *61*, No. e202203358.

(15) Yu, W.; Deschaume, O.; Dedroog, L.; Garcia Abrego, C. J. G.; Zhang, P. F.; Wellens, J.; de Coene, Y.; Jooken, S.; Clays, K.; Thielemans, W.; et al. Light-Addressable Nanocomposite Hydrogels Allow Plasmonic Actuation and in Situ Temperature Monitoring in 3D Cell Matrices. *Adv. Funct. Mater.* **2022**, *32*, 2108234.
(16) Manzeli, S.; Ovchinnikov, D.; Pasquier, D.; Yazyev, O. V.; Kis, A. 2D Transition Metal Dichalcogenides. *Nat. Rev. Mater.* **2017**, *2*, 17033.
(17) Mak, K. F.; Shan, J. Photonics and Optoelectronics of 2D Semiconductor Transition Metal Dichalcogenides. *Nat. Photonics* **2016**, *10*, 216−226.
(18) Lin, Y.; Ling, X.; Yu, L.; Huang, S.; Hsu, A. L.; Lee, Y.-H.; Kong, J.; Dresselhaus, M. S.; Palacios, T. Dielectric Screening of Excitons and Trions in Single-Layer MoS_2. *Nano Lett.* **2014**, *14*, 5569−5576.
(19) Mao, N.; Chen, Y.; Liu, D.; Zhang, J.; Xie, L. Solvatochromic Effect on the Photoluminescence of MoS_2 Monolayers. *Small* **2013**, *9*, 1312−1315.
(20) Wang, M.; Krasnok, A.; Zhang, T.; Scarabelli, L.; Liu, H.; Wu, Z.; Liz-Marzán, L. M.; Terrones, M.; Alù, A.; Zheng, Y. Tunable Fano Resonance and Plasmon-Exciton Coupling in Single Au Nanotriangles on Monolayer WS_2 at Room Temperature. *Adv. Mater.* **2018**, *30*, 1705779.
(21) Ma, N.; Jena, D. Charge Scattering and Mobility in Atomically Thin Semiconductors. *Phys. Rev. X* **2014**, *4*, 011043.
(22) Buscema, M.; Steele, G. A.; van der Zant, H. S. J.; Castellanos-Gomez, A. The Effect of the Substrate on the Raman and Photoluminescence Emission of Single-Layer MoS_2. *Nano Res.* **2014**, *7*, 561−571.
(23) Zheng, X.; Wei, Y.; Zhang, X.; Wei, Z.; Luo, W.; Guo, X.; Liu, J.; Peng, G.; Cai, W.; Huang, H.; et al. Symmetry Engineering Induced in-Plane Polarization in MoS_2 through van der Waals Interlayer Coupling. *Adv. Funct. Mater.* **2022**, *32*, 2202658.
(24) Li, S. L.; Wakabayashi, K.; Xu, Y.; Nakaharai, S.; Komatsu, K.; Li, W. W.; Lin, Y. F.; Aparecido-Ferreira, A.; Tsukagoshi, K. Thickness-Dependent Interfacial Coulomb Scattering in Atomically Thin Field-Effect Transistors. *Nano Lett.* **2013**, *13*, 3546−3552.
(25) Phuc, H. V.; Hieu, N. N.; Hoi, B. D.; Hieu, N. V.; Thu, T. V.; Hung, N. M.; Ilyasov, V. V.; Poklonski, N. A.; Nguyen, C. V. Tuning the Electronic Properties, Effective Mass and Carrier Mobility of MoS_2 Monolayer by Strain Engineering: First-Principle Calculations. *J. Electron. Mater.* **2018**, *47*, 730−736.
(26) Radisavljevic, B.; Kis, A. Mobility Engineering and a Metal-Insulator Transition in Monolayer MoS_2. *Nat. Mater.* **2013**, *12*, 815−820.
(27) Hu, G. W.; Hong, X. M.; Wang, K.; Wu, J.; Xu, H. X.; Zhao, W. C.; Liu, W. W.; Zhang, S.; Garcia-Vidal, F.; Wang, B.; et al. Coherent Steering of Nonlinear Chiral Valley Photons with a Synthetic Au-WS_2 Metasurface. *Nat. Photonics* **2019**, *13*, 467−472.
(28) Nam, N. N.; Bui, T. L.; Son, S. J.; Joo, S. W. Ultrasonication-Induced Self-Assembled Fixed Nanogap Arrays of Monomeric Plasmonic Nanoparticles inside Nanopores. *Adv. Funct. Mater.* **2019**, *29*, 1809146.
(29) Sarkar, S.; Gupta, V.; Tsuda, T.; Gour, J.; Singh, A.; Aftenieva, O.; Steiner, A. M.; Hoffmann, M.; Kumar, S.; Fery, A.; et al. Plasmonic Charge Transfers in Large-Scale Metallic and Colloidal Photonic Crystal Slabs. *Adv. Funct. Mater.* **2021**, *31*, 2011099.
(30) Niu, Y.; Xu, H.; Wei, H. Unified Scattering and Photoluminescence Spectra for Strong Plasmon-Exciton Coupling. *Phys. Rev. Lett.* **2022**, *128*, 167402.

https://doi.org/10.1021/acs.jpcc.2c05598
J. Phys. Chem. C 2022, 126, 15864−15872